Engineering Weyl Phases and Nonlinear Hall Effects in T_d-$MoTe_2$

Sobhit Singh,* Jinwoong Kim, Karin M. Rabe, and David Vanderbilt
Department of Physics and Astronomy, Rutgers University, Piscataway, New Jersey 08854-8019, USA

(Received 10 February 2020; revised 9 July 2020; accepted 23 June 2020; published 21 July 2020)

$MoTe_2$ has recently attracted much attention due to the observation of pressure-induced superconductivity, exotic topological phase transitions, and nonlinear quantum effects. However, there has been debate on the intriguing structural phase transitions among various observed phases of $MoTe_2$ and their connection to the underlying topological electronic properties. In this work, by means of density-functional theory calculations, we investigate the structural phase transition between the polar T_d and nonpolar 1T′ phases of $MoTe_2$ in reference to a hypothetical high-symmetry T_0 phase that exhibits higher-order topological features. In the T_d phase we obtain a total of 12 Weyl points, which can be created/annihilated, dynamically manipulated, and switched by tuning a polar phonon mode. We also report the existence of a tunable nonlinear Hall effect in T_d-$MoTe_2$ and propose the use of this effect as a probe for the detection of polarity orientation in polar (semi)metals. By studying the role of dimensionality, we identify a configuration in which a nonlinear surface response current emerges. The potential technological applications of the tunable Weyl phase and the nonlinear Hall effect are discussed.

DOI: 10.1103/PhysRevLett.125.046402

There has recently been substantial progress in understanding the structural and topological electronic properties of $MoTe_2$ [1–22]. Most of the previous theoretical and experimental studies have focused on the characterization of the distinct phases of $MoTe_2$ and reported the observation of various novel quantum phenomena such as extremely large magnetoresistance [12–15], Weyl semimetallic phase [23–31], higher-order topological phase [32–34], superconductivity [35,36], tunable polar/phase domain walls [9–11], and various kinds of Hall effects [37–42]. In contrast, the total number and location of Weyl fermions in $MoTe_2$ are still under debate [23–31,43–45], and the link between the higher-order topological phase (1T′) and the Weyl phase (T_d) has remained elusive. Specifically, a systematic connection among these electronic phases, in the context of the potential energy surface profile and crystal symmetries, has been relatively unexplored in the literature.

In this Letter, by means of *ab initio* density-functional theory (DFT) calculations, we first investigate the structural phase transition between the polar T_d and nonpolar 1T′ phases of $MoTe_2$ using a hypothetical reference phase T_0 introduced by us in the context of the experimental results in Ref. [11]. In particular, we focus on the electronic phase transitions occurring in the vicinity of the T_0 phase. We study the evolution of the Weyl points (WPs) in the polar phase along the polarity reversal path and demonstrate that a higher-order topological phase naturally appears when all WPs annihilate each other at zero polar distortion in the reference phase T_0. We also report on the existence of a tunable nonlinear Hall effect (NLHE) and propose that the NLHE can be used to detect polarization direction and switching in polar metals or semimetals, especially those with strong sources of Berry curvature near the Fermi energy. Such a tunable NLHE could lead to electrically switchable circular photogalvanic [40,46], bulk rectification [47], and chiral polaritonic effects [48]. Finally, we discuss the role of dimensionality on this effect and argue that the surface termination along the (001) direction leads to the manifestation of a nonlinear surface response current solely arising due to the broken symmetries at the surface.

$MoTe_2$ crystallizes in three distinct phases: (i) 2H (hexagonal, $P6_3/mmc$), (ii) 1T′ (monoclinic, $P2_1/m$), and (iii) T_d (orthorhombic, $Pnm2_1$) [9,17,49]. In all three phases, Mo and Te atoms form Te-Mo-Te triple layers, which stack along the c axis and interact *via* weak van der Waals interactions. The Te atoms form symmetrical polyhedra in the hexagonal 2H phase, whereas these polyhedra are markedly distorted in the 1T′ and T_d phases [11], as shown in Figs. 1(a) and 1(c). Both phases are quite similar, except for the fact that 1T′ is monoclinic ($\beta \neq 90$) while T_d is orthorhombic ($\alpha = \beta = \gamma = 90$). In both phases, Mo atoms dimerize, forming long-short bonds along the $\vec{a}$ lattice vector and zigzag Mo-Mo metallic bonds running along the $\vec{b}$ direction.

We notice an interesting symmetry between the Mo-Te polyhedra [see light gray rectangles in Fig. 1(c)] of alternating triple layers. These polyhedra alternatively adopt either clockwise or counterclockwise twist (as viewed along $\vec{b}$) in the alternating triple layers. In the T_d phase, adjacent layers are connected by $\mathcal{M}_x|\{\mathcal{T}[(\vec{a}/2)(1+\lambda)]\}$ symmetry operation, where $\mathcal{M}_x$ is a vertical mirror, $\mathcal{T}(\vec{a}/2)$ denotes translation by $\vec{a}/2$, and λ denotes an interlayer displacement along $\vec{a}$, as shown in Fig. 1(c).

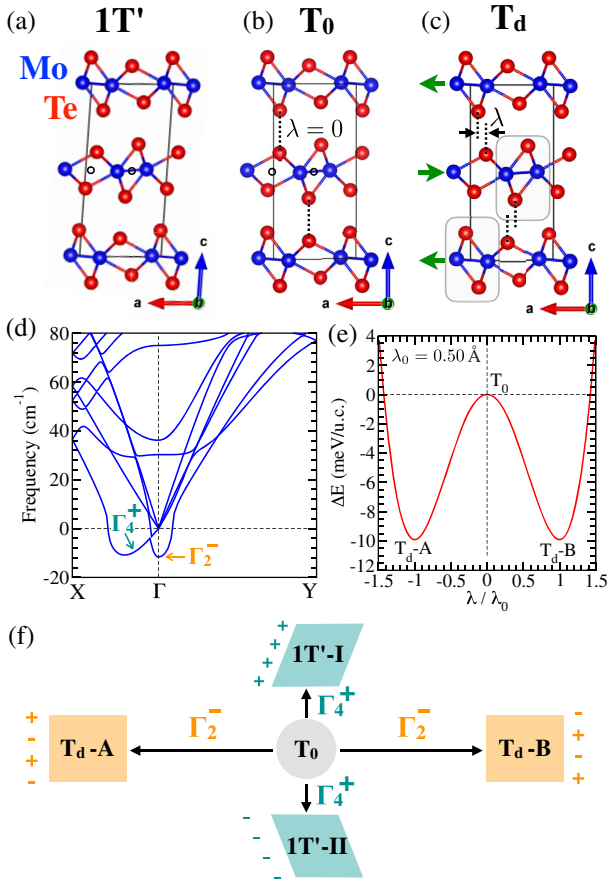

FIG. 1. Crystal structure of $MoTe_2$ in (a) 1T′, (b) designed T_0, and (c) T_d phases. Green arrows denote the interlayer displacement direction parallel (+) or antiparallel (−) to $\vec{a}$, and λ represents the interlayer displacement parameter (see text). Hollow circles '∘' mark the inversion centers in the 1T′ and T_0 phases. (d) The phonon band structure of T_0 phase shown within $[-20, 80]$ cm^{-1}. (e) The double-well potential energy profile of T_0 phase as a function of the inversion symmetry breaking parameter λ. (f) A schematic representation showing the link between all T_d and 1T′ phases *via* the reference structure T_0 [11].

The main cause of the nonzero λ is the presence of steric interactions between Te atoms in the adjacent triple layers, which drive an in-plane shift of the alternating layers along $\vec{a}$ so as to increase the separation between these atoms. Taking the above facts into account, we define a nonpolar high-symmetry phase T_0 (*Pnma*) having $\lambda = 0$, as shown in Fig. 1(b).

Figure 1(d) shows an enlarged phonon spectrum of the T_0 phase. The full phonon spectra of T_0, 1T′, and T_d phases together with all the theoretical details are given in the Supplemental Material (SM) [50]. We notice only two phonon instabilities in the T_0 phase: (i) an unstable optical zone center phonon mode (Γ_2^-), and (ii) a linearly dispersing unstable phonon branch along Γ-X direction indicating an elastic instability (Γ_4^+). The first instability, Γ_2^-, breaks the inversion symmetry of the T_0 phase and corresponds to an in-plane optical vibration of the alternating triple layers. By modulating T_0 phase along Γ_2^- mode, we obtain a double-well potential energy profile with two local minima at $\lambda = \pm 0.50$ Å, as shown in Fig. 1(e). These local minima belong to the two polar variants of the T_d phase, which we refer as T_d-A and T_d-B. The interlayer displacement pattern of the alternating Mo-Te triple layers in the T_d-A and T_d-B phases is $-+-+\ldots$ and $+-+-\ldots$, respectively, thus ensuring the orthogonality of the T_d phase. On the other hand, the elastic instability (Γ_4^+ mode) causes a shear distortion of the unit cell, resulting in two ferroelastic twin phases, 1T′-I and 1T′-II, corresponding to the interlayer displacement pattern of $++++\ldots$ and $----\ldots$, respectively (details in SM [50]). A schematic connection among the T_d, 1T′, and T_0 phases is shown in Fig. 1(f).

Due to the broken inversion symmetry requirement, the path connecting the 1T'-I and 1T'-II phases cannot access the Weyl phase. Therefore, we focus on the T_d-A → T_d-B path, investigating the subtle changes in the electronic band structure that occur there. Without spin-orbit coupling (SOC), the lowest conduction band and the highest valence band cross each other near the Fermi level (E_F), forming gapless nodal loops [26] above and below E_F, as marked by arrows in Fig. 2(b) [63]. Inclusion of SOC destroys the nodal loops and results in discrete WPs formed away from the high-symmetry directions near the Fermi level. We find that there are two sets of WPs: (i) W1 WPs lying at $E_F + 0.108$ eV (in the $k_z = 0$ plane), and (ii) W2 WPs lying at $E_F - 0.038$ eV (off the $k_z = 0$ plane). Both W1 and W2 WPs have type-II nature, as shown in Fig. 2(c). However, W1 WPs have a stronger tilting of Weyl cone compared to W2. There are a total of 12 WPs (four W1 and eight W2) in the full Brillouin zone (BZ), as shown in Fig. 2(d). Coordinates of all WPs are provided in the SM [50]. The T_d-A and T_d-B phases host exactly the same number of WPs at the same coordinates in momentum and energy but with reversed chirality.

Motivated by the above results, we investigate the evolution of the WPs along the T_d-A → T_0 → T_d-B path as a function of λ. We observe that WPs get created in pairs as we move away from the T_d-A phase. The total number of WPs increases from 12 to 16 and then 20, 24, 28, and 32 as we vary $|\lambda/\lambda_0|$ from 1.0 to 0.92, 0.88, 0.79, 0.72, and 0.63, respectively ($\lambda_0 = 0.50$ Å) [50]. The maximum number of obtained WPs is 32. This finding explains why previous authors reported such different counts of the number of Weyl points [23–31,43–45] and reveals that the total number of WPs in $MoTe_2$ is very sensitive to the lattice distortions [23]. As we further tune $|\lambda/\lambda_0|$, the WPs move toward their opposite partners in momentum space and start pair-annihilating, leaving no remaining WPs at $|\lambda/\lambda_0| = 0$ (at T_0 phase).

Due to the absence of WPs and the presence of a double band inversion at the Γ point, the T_0 phase turns into a

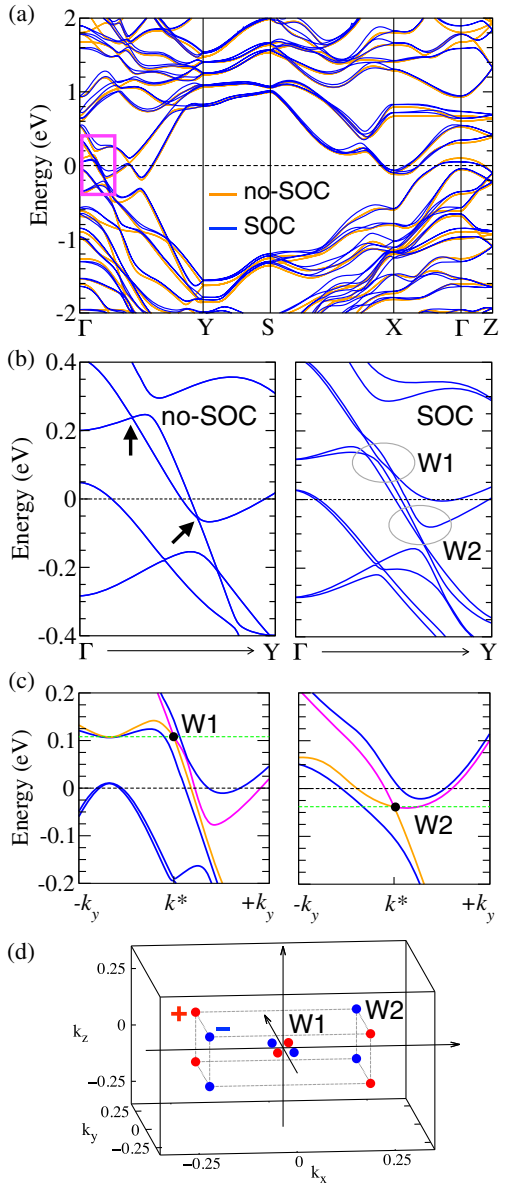

FIG. 2. (a) Electronic band structure of T_d-$MoTe_2$ calculated with (blue) and without (orange) SOC. (b) Enlarged view of bands calculated near the Fermi level E_F along the Γ-Y path highlighted by the magenta rectangle in (a). Gray ovals in the right panel of (b) show the regions near which Weyl crossings occur. (c) Band dispersions (with SOC) along a momentum cut parallel to k_y passing through the WP (black dots) in question [50]; both W1 and W2 are of type II. The dotted black line represents E_F, and the green dotted line marks the energy of WPs situated at k^*. (d) Distribution of all WPs in the BZ for the T_d-A phase; red/blue dots depict $+/-$ chiralities of the WPs.

second-order topological insulator similar to the 1T′ phase [32,33]. Notably, we find that both the T_0 and 1T′ phases belong to a strong topological class 20 as classified in Ref. [51] having topological invariant $z_4 = 2$. As we cross the T_0 phase and migrate toward the T_d-B phase, the WPs systematically start reappearing, and the aforementioned process repeats but with the switched chirality of WPs [65]. The pairwise creation/annihilation of WPs causes abrupt changes in the Berry curvature and Fermi-surface geometry yielding a nonzero Berry curvature dipole moment (BCDM) [66] and, as a result, an NLHE in T_d-$MoTe_2$ [41], as we discuss below.

In the study of the nonlinear quantum Hall effect [66–69], a transverse current is predicted to be generated by a harmonically oscillating electric field $E_c = \mathrm{Re}\{\mathcal{E}_c e^{i\omega t}\}$ in the absence of inversion symmetry. The response current up to second order reads $j_a = \mathrm{Re}\{j_a^0 + j_a^{2\omega} e^{2i\omega t}\}$, where a rectified current $j_a^0 = \chi_{abc}\mathcal{E}_b\mathcal{E}_c^*$ and a second-harmonic current $j_a^{2\omega} = \chi_{abc}\mathcal{E}_b\mathcal{E}_c$ depend on the nonlinear conductivity tensor χ_{abc}, where $a, b, c \in \{x, y, z\}$. The nonlinear conductivity tensor associated with the BCDM (D_{bd}) can be written as

$$\chi_{abc}(\omega) = -\varepsilon_{adc}\frac{e^3\tau}{2(1+i\omega\tau)}D_{bd}, \tag{1}$$

where ε_{abc} is the rank-three Levi–Civita symbol and τ is the relaxation time. The D_{bd} is obtained by integrating Berry curvature weighted by the Cartesian component of the group velocity on the Fermi surface according to

$$D_{bd} = \oint_{\mathrm{FS}} \frac{d^2\boldsymbol{k}}{(2\pi)^3}\sum_n v_b^n(\boldsymbol{k})\Omega_d^n(\boldsymbol{k}), \tag{2}$$

where $v_b^n(\boldsymbol{k}) = \partial_{k_b}E_{n\boldsymbol{k}}/|\nabla_{\boldsymbol{k}}E_{n\boldsymbol{k}}|$ is a normalized group velocity component for band n, and $\boldsymbol{\Omega}^n$ is the Berry curvature pseudovector defined *via* $\Omega_{bc}^n = \varepsilon_{abc}\Omega_a^n$. The superscripts represent band indices. We compute the Berry curvature using the Kubo formula

$$\Omega_{ab}^n(\boldsymbol{k}) = -2\hbar^2\sum_{m\neq n}\mathrm{Im}\frac{\langle n\boldsymbol{k}|\hat{v}_a|m\boldsymbol{k}\rangle\langle m\boldsymbol{k}|\hat{v}_b|n\boldsymbol{k}\rangle}{(E_{n\boldsymbol{k}}-E_{m\boldsymbol{k}})^2+\delta^2}, \tag{3}$$

where $\hat{v}_a$ is the velocity operator and $\delta = 0.1$ meV is a broadening term (see [70] for numerical details).

In the presence of inversion symmetry, i.e., the case of 1T′-$MoTe_2$, the BCDM completely vanishes. Instead, in the polar T_d phase, a nonvanishing BCDM is allowed [66,71]. T_d-$MoTe_2$ exhibits simple mirror $\mathcal{M}_y$ and glide mirror $\mathcal{M}_x\mathcal{T}(\vec{c}/2)$ symmetries, exerting constraints on the BCDM tensor. For instance, $\mathcal{M}_y$, a mirror plane normal to the chain direction, forces the group velocity v_a and Berry curvature Ω_b to obey

$$\mathcal{M}_y\colon (v_x, v_y, v_z) \to (v_x, -v_y, v_z) \tag{4}$$

$$(\Omega_x, \Omega_y, \Omega_z) \to (-\Omega_x, \Omega_y, -\Omega_z). \tag{5}$$

Here, the v_i denotes group velocity for a particular band at a particular $\boldsymbol{k}$. Thus, under the $\mathcal{M}_y$ symmetry operation, all components of the BCDM tensor vanish except for the D_{xy},

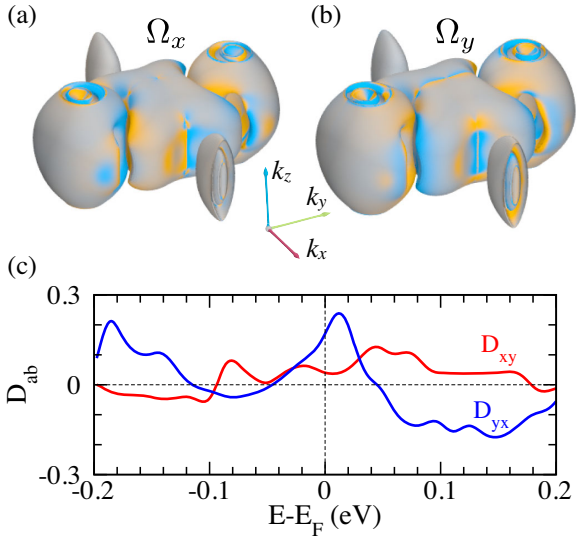

FIG. 3. Calculated Berry curvature (a) Ω_x and (b) Ω_y on the Fermi surface of $MoTe_2$ in T_d-A phase. Yellow (Blue) color represents positive (negative) Berry curvature. (c) Calculated BCDM of $MoTe_2$ in T_d-A phase. The nonvanishing D_{xy} and D_{yz} terms are plotted with respect to the chemical potential.

D_{yx}, D_{yz}, and D_{zy} terms. A further consideration of $\mathcal{M}_x\mathcal{T}(\vec{c}/2)$ symmetry eliminates the D_{yz} and D_{zy} terms as well. Thus, only two terms, D_{xy} and D_{yx}, survive in T_d-$MoTe_2$.

The nonvanishing nature of the D_{xy} and D_{yx} terms can be anticipated from the Berry curvature distribution plot on the Fermi surface [Figs. 3(a) and 3(b)]. Because of the complex metallic bands with anisotropic group velocities in type-II Weyl semimetals, the Fermi surface has significant Berry curvature even away from the WPs. This renders the BCDM more sensitive to the chemical potential than for type-I Weyl semimetals [72]. Figure 3(c) shows that D_{yx} is peaked near the Fermi level, while D_{xy} exhibits oscillating behavior. At E_F, D_{xy} and D_{yx} are estimated to be 0.04 and 0.17, respectively [74]. These values are smaller than the corresponding $D_{xy} = 0.8$ and $D_{yx} = -0.7$ reported for T_d-$MoTe_2$ by Zhang *et al.* [41]. The main reason behind this difference is the strong sensitivity of the Fermi surface to the on-site Hubbard U of Mo $4d$ electrons [43,44], which was not taken into account in the previous study [75].

From Eq. (1), the nonlinear conductivity tensor has nonzero terms $\chi_{xxz} = -\chi_{zxx}$ associated with D_{xy}, and $\chi_{zyy} = -\chi_{yyz}$ associated with D_{yx}. In view of the significant peak in D_{yx} near E_F, one interesting measurement would be the observation of a transverse current j_z induced by an oscillating electric field along y direction. In the $\omega \to 0$ limit, an external electric field applied along the y direction, i.e., the chain direction, generates an out-of-plane current $j_z^0 = 2\chi_{zyy}|\mathcal{E}_y|^2$. If one can raise the electron chemical potential *via* gating, the transverse current j_z^0 is predicted to rapidly reach its maximum and then decrease and eventually reverse its sign.

Here, we stress that a structural transition from the T_d-A to T_d-B phase flips the sign of D_{ab} while keeping its magnitude intact, thus allowing one to distinguish between the two variants of polar T_d phases [76]. For this purpose, observation of D_{xy} via $j_z^0 = 2\chi_{zxx}|\mathcal{E}_x|^2$ may be most suitable, since the sign of D_{xy} is less sensitive to the electron chemical potential.

An interesting aspect of the nonlinear Hall conductivity in this system is that, because the surfaces have lower symmetry than the bulk, new components of the D tensor are activated at the surface. In particular, the glide mirror $\mathcal{M}_x\mathcal{T}(\vec{c}/2)$ is broken at the (001) cleavage surface. Recall that the D_{yz} and D_{zy} tensor elements were argued to vanish in the bulk because of this glide mirror, but they need not vanish at the surface. Thus, response currents associated with the conductivity tensor elements $\chi_{yyx} = -\chi_{xyy}$ and $\chi_{xzz} = -\chi_{zzx}$ are allowed. While we can confidently predict the existence of such currents, we are not currently in a position to compute the surface D tensors quantitatively. This observation thus provides a challenge for future efforts at both theoretical prediction and experimental detection of surface nonlinear Hall responses.

We may also consider the symmetries that remain in the exfoliated few-layer limit. In fact, the $\chi_{yyx} = -\chi_{xyy} \propto D_{yz}$ tensor elements are the only ones to survive in this limit. The other terms, proportional to Ω_x or Ω_y, are not well defined in two dimensions. Therefore, measuring the in-plane nonlinear Hall conductivity of $MoTe_2$ with respect to the film thickness may reveal a noticeable transition from the film to the surface responses.

In principle, one can utilize the nonlinear response current generated due to the rapid fluctuation of D_{yx} and its sign reversal near the Fermi level as a function of the chemical potential to devise a nonlinear Hall transistor for practical applications. Moreover, recent experiments [18,77] demonstrated an ultrafast optical control over T_d and 1T′ structural phase transitions; hence, an ultrafast topological optical switch can be designed using the nonlinear quantum Hall property of $MoTe_2$, where T_d (1T′) phase can act as an ON (OFF) state.

Unlike in polar insulators, in which the switching of polarity is immediately manifested in a polarization switching current, a corresponding experimental response is missing in the case of polar metals. Here, we propose that the NLHE may serve as a potential experimental response to detect the polarization direction/switching in polar metals, particularly, in nonmagnetic Weyl semimetals. As demonstrated above, the polarization switching in Weyl semimetals is always accompanied by the reversal of the nonlinear Hall response.

In summary, we explain the intricate structural phase transitions in $MoTe_2$ by defining a high-symmetry nonpolar phase T_0 that exhibits a higher-order topology. We unveil the connection between the Weyl phase and the higher-order topological phase in $MoTe_2$. We report that

WPs can be readily created/annihilated, manipulated, and switched by controlling the structural phase transitions between the two polar variants of the T_d phase. We also report on the presence of a tunable NLHE in T_d-$MoTe_2$ and discuss the potential applications of this effect in designing ultrafast topological optical switches and transistors. Lastly, we propose that the NLHE can be utilized as a potential experimental response to detect polarization direction/switching in polar metals or semimetals that inherit large concentrations of Berry curvature near the Fermi energy, e.g., in nonmagnetic Weyl semimetals.

We thank Fei-ting Huang and Sang-Wook Cheong for fruitful discussions. This work was supported by ONR Grants No. N00014-16-1-2951 and No. N00014-19-1-2073.

*Corresponding author.
sobhit.singh@rutgers.edu

[1] Q. H. Wang, K. Kalantar-Zadeh, A. Kis, J. N. Coleman, and M. S. Strano, Nat. Nanotechnol. **7**, 699 (2012).
[2] D. H. Keum, S. Cho, J. H. Kim, D.-H. Choe, H.-J. Sung, M. Kan, H. Kang, J.-Y. Hwang, S. W. Kim, H. Yang, K. J. Chang, and Y. H. Lee, Nat. Phys. **11**, 482 (2015).
[3] K. Zhang, C. Bao, Q. Gu, X. Ren, H. Zhang, K. Deng, Y. Wu, Y. Li, J. Feng, and S. Zhou, Nat. Commun. **7**, 13552 (2016).
[4] Y. Wang, J. Xiao, H. Zhu, Y. Li, Y. Alsaid, K. Y. Fong, Y. Zhou, S. Wang, W. Shi, Y. Wang, A. Zettl, E. J. Reed, and X. Zhang, Nature (London) **550**, 487 (2017).
[5] G. Wang, A. Chernikov, M. M. Glazov, T. F. Heinz, X. Marie, T. Amand, and B. Urbaszek, Rev. Mod. Phys. **90**, 021001 (2018).
[6] A. N. Berger, E. Andrade, A. Kerelsky, D. Edelberg, J. Li, Z. Wang, L. Zhang, J. Kim, N. Zaki, J. Avila, C. Chen, M. C. Asensio, S.-W. Cheong, B. A. Bernevig, and A. N. Pasupathy, npj Quantum Mater. **3**, 2 (2018).
[7] W. Jin *et al.*, Phys. Rev. B **98**, 144114 (2018).
[8] C. Si, D. Choe, W. Xie, H. Wang, Z. Sun, J. Bang, and S. Zhang, Nano Lett. **19**, 3612 (2019).
[9] C. Heikes, I.-L. Liu, T. Metz, C. Eckberg, P. Neves, Y. Wu, L. Hung, P. Piccoli, H. Cao, J. Leao, J. Paglione, T. Yildirim, N. P. Butch, and W. Ratcliff, Phys. Rev. Mater. **2**, 074202 (2018).
[10] S. Yuan, X. Luo, H. L. Chan, C. Xiao, Y. Dai, M. Xie, and J. Hao, Nat. Commun. **10**, 1775 (2019).
[11] F.-T. Huang, S. J. Lim, S. Singh, J. Kim, L. Zhang, J.-W. Kim, M.-W. Chu, K. M. Rabe, D. Vanderbilt, and S.-W. Cheong, Nat. Commun. **10**, 4211 (2019).
[12] F. C. Chen, H. Y. Lv, X. Luo, W. J. Lu, Q. L. Pei, G. T. Lin, Y. Y. Han, X. B. Zhu, W. H. Song, and Y. P. Sun, Phys. Rev. B **94**, 235154 (2016).
[13] Q. L. Pei, W. J. Meng, X. Luo, H. Y. Lv, F. C. Chen, W. J. Lu, Y. Y. Han, P. Tong, W. H. Song, Y. B. Hou, Q. Y. Lu, and Y. P. Sun, Phys. Rev. B **96**, 075132 (2017).
[14] S. Thirupathaiah, R. Jha, B. Pal, J. S. Matias, P. K. Das, P. K. Sivakumar, I. Vobornik, N. C. Plumb, M. Shi, R. A. Ribeiro, and D. D. Sarma, Phys. Rev. B **95**, 241105(R) (2017).
[15] S. Lee, J. Jang, S.-I. Kim, S.-G. Jung, J. Kim, S. Cho, S. W. Kim, J. Y. Rhee, K.-S. Park, and T. Park, Sci. Rep. **8**, 13937 (2018).
[16] S.-Y. Chen, T. Goldstein, D. Venkataraman, A. Ramasubramaniam, and J. Yan, Nano Lett. **16**, 5852 (2016).
[17] H.-J. Kim, S.-H. Kang, I. Hamada, and Y.-W. Son, Phys. Rev. B **95**, 180101(R) (2017).
[18] M. Y. Zhang, Z. X. Wang, Y. N. Li, L. Y. Shi, D. Wu, T. Lin, S. J. Zhang, Y. Q. Liu, Q. M. Liu, J. Wang, T. Dong, and N. L. Wang, Phys. Rev. X **9**, 021036 (2019).
[19] R. He, S. Zhong, H. H. Kim, G. Ye, Z. Ye, L. Winford, D. McHaffie, I. Rilak, F. Chen, X. Luo, Y. Sun, and A. W. Tsen, Phys. Rev. B **97**, 041410(R) (2018).
[20] P. Tsipas, S. Fragkos, D. Tsoutsou, C. Alvarez, R. Sant, G. Renaud, H. Okuno, and A. Dimoulas, Adv. Funct. Mater. **28**, 1802084 (2018).
[21] Y. Tao, J. A. Schneeloch, C. Duan, M. Matsuda, S. E. Dissanayake, A. A. Aczel, J. A. Fernandez-Baca, F. Ye, and D. Louca, Phys. Rev. B **100**, 100101(R) (2019).
[22] S. Dissanayake, C. Duan, J. Yang, J. Liu, M. Matsuda, C. Yue, J. A. Schneeloch, J. C. Y. Teo, and D. Louca, npj Quantum Mater. **4**, 45 (2019).
[23] Y. Sun, S.-C. Wu, M. N. Ali, C. Felser, and B. Yan, Phys. Rev. B **92**, 161107(R) (2015).
[24] A. A. Soluyanov, D. Gresch, Z. Wang, Q. Wu, M. Troyer, X. Dai, and B. A. Bernevig, Nature (London) **527**, 495 (2015).
[25] L. Huang, T. M. McCormick, M. Ochi, Z. Zhao, M.-T. Suzuki, R. Arita, Y. Wu, D. Mou, H. Cao, J. Yan, N. Trivedi, and A. Kaminski, Nat. Mater. **15**, 1155 (2016).
[26] Z. Wang, D. Gresch, A. A. Soluyanov, W. Xie, S. Kushwaha, X. Dai, M. Troyer, R. J. Cava, and B. A. Bernevig, Phys. Rev. Lett. **117**, 056805 (2016).
[27] K. Deng, G. Wan, P. Deng, K. Zhang, S. Ding, E. Wang, M. Yan, H. Huang, H. Zhang, Z. Xu, J. Denlinger, A. Fedorov, H. Yang, W. Duan, H. Yao, Y. Wu, S. Fan, H. Zhang, X. Chen, and S. Zhou, Nat. Phys. **12**, 1105 (2016).
[28] A. Tamai, Q. S. Wu, I. Cucchi, F. Y. Bruno, S. Riccò, T. K. Kim, M. Hoesch, C. Barreteau, E. Giannini, C. Besnard, A. A. Soluyanov, and F. Baumberger, Phys. Rev. X **6**, 031021 (2016).
[29] D. Rhodes, R. Schönemann, N. Aryal, Q. Zhou, Q. R. Zhang, E. Kampert, Y.-C. Chiu, Y. Lai, Y. Shimura, G. T. McCandless, J. Y. Chan, D. W. Paley, J. Lee, A. D. Finke, J. P. C. Ruff, S. Das, E. Manousakis, and L. Balicas, Phys. Rev. B **96**, 165134 (2017).
[30] A. Crepaldi *et al.*, Phys. Rev. B **96**, 241408(R) (2017).
[31] A. Zhang, X. Ma, C. Liu, R. Lou, Y. Wang, Q. Yu, Y. Wang, T.-l. Xia, S. Wang, L. Zhang, X. Wang, C. Chen, and Q. Zhang, Phys. Rev. B **100**, 201107(R) (2019).
[32] Z. Wang, B. J. Wieder, J. Li, B. Yan, and B. A. Bernevig, Phys. Rev. Lett. **123**, 186401 (2019).
[33] F. Tang, H. C. Po, A. Vishwanath, and X. Wan, Nat. Phys. **15**, 470 (2019).
[34] M. Ezawa, Sci. Rep. **9**, 5286 (2019).
[35] H. Takahashi, T. Akiba, K. Imura, T. Shiino, K. Deguchi, N. K. Sato, H. Sakai, M. S. Bahramy, and S. Ishiwata, Phys. Rev. B **95**, 100501(R) (2017).
[36] Y. Qi *et al.*, Nat. Commun. **7**, 11038 (2016).

[37] F. C. Chen, X. Luo, J. Yan, Y. Sun, H. Y. Lv, W. J. Lu, C. Y. Xi, P. Tong, Z. G. Sheng, X. B. Zhu, W. H. Song, and Y. P. Sun, Phys. Rev. B **98**, 041114(R) (2018).

[38] Y. Zhang, J. van den Brink, C. Felser, and B. Yan, 2D Mater. **5**, 044001 (2018).

[39] X. Qian, J. Liu, L. Fu, and J. Li, Science **346**, 1344 (2014).

[40] S. Lim, C. R. Rajamathi, V. Süß, C. Felser, and A. Kapitulnik, Phys. Rev. B **98**, 121301(R) (2018).

[41] Y. Zhang, Y. Sun, and B. Yan, Phys. Rev. B **97**, 041101(R) (2018).

[42] J. Zhou, J. Qiao, A. Bournel, and W. Zhao, Phys. Rev. B **99**, 060408(R) (2019).

[43] N. Xu, Z. W. Wang, A. Magrez, P. Bugnon, H. Berger, C. E. Matt, V. N. Strocov, N. C. Plumb, M. Radovic, E. Pomjakushina, K. Conder, J. H. Dil, J. Mesot, R. Yu, H. Ding, and M. Shi, Phys. Rev. Lett. **121**, 136401 (2018).

[44] N. Aryal and E. Manousakis, Phys. Rev. B **99**, 035123 (2019).

[45] A. P. Weber, P. Rüßmann, N. Xu, S. Muff, M. Fanciulli, A. Magrez, P. Bugnon, H. Berger, N. C. Plumb, M. Shi, S. Blügel, P. Mavropoulos, and J. H. Dil, Phys. Rev. Lett. **121**, 156401 (2018).

[46] S.-Y. Xu, Q. Ma, H. Shen, V. Fatemi, S. Wu, T.-R. Chang, G. Chang, A. M. M. Valdivia, C.-K. Chan, Q. D. Gibson, J. Zhou, Z. Liu, K. Watanabe, T. Taniguchi, H. Lin, R. J. Cava, L. Fu, N. Gedik, and P. Jarillo-Herrero, Nat. Phys. **14**, 900 (2018).

[47] T. Ideue, K. Hamamoto, S. Koshikawa, M. Ezawa, S. Shimizu, Y. Kaneko, Y. Tokura, N. Nagaosa, and Y. Iwasa, Nat. Phys. **13**, 578 (2017).

[48] D. N. Basov, M. M. Fogler, and F. J. García de Abajo, Science **354**, aag1992 (2016).

[49] R. Clarke, E. Marseglia, and H. P. Hughes, Philos. Mag. B **38**, 121 (1978).

[50] See Supplemental Material (SM) at http://link.aps.org/supplemental/10.1103/PhysRevLett.125.046402 for numerical details and for additional information regarding the calculated phonon spectrum, potential energy barrier profile for 1T′ twin phases, electronic band structure, evolution of WPs and BCDM as a function of λ, coordinates of all WPs, and higher-order topological classification of T_0 and 1T′ phases. SM comprises Refs. [6,16,32,43,44,49,51–62].

[51] M. G. Vergniory, L. Elcoro, C. Felser, N. Regnault, B. A. Bernevig, and Z. Wang, Nature (London) **566**, 480 (2019).

[52] G. Kresse and J. Furthmüller, Phys. Rev. B **54**, 11169 (1996).

[53] G. Kresse and J. Furthmüller, Comput. Mater. Sci. **6**, 15 (1996).

[54] P. E. Blöchl, Phys. Rev. B **50**, 17953 (1994).

[55] G. Kresse and D. Joubert, Phys. Rev. B **59**, 1758 (1999).

[56] J. P. Perdew, A. Ruzsinszky, G. I. Csonka, O. A. Vydrov, G. E. Scuseria, L. A. Constantin, X. Zhou, and K. Burke, Phys. Rev. Lett. **100**, 136406 (2008).

[57] S. L. Dudarev, G. A. Botton, S. Y. Savrasov, C. J. Humphreys, and A. P. Sutton, Phys. Rev. B **57**, 1505 (1998).

[58] X.-J. Yan, Y.-Y. Lv, L. Li, X. Li, S.-H. Yao, Y.-B. Chen, X.-P. Liu, H. Lu, M.-H. Lu, and Y.-F. Chen, npj Quantum Mater. **2**, 31 (2017).

[59] S. Singh, I. Valencia-Jaime, O. Pavlic, and A. H. Romero, Phys. Rev. B **97**, 054108 (2018).

[60] A. Togo and I. Tanaka, Scr. Mater. **108**, 1 (2015).

[61] Q. Wu, S. Zhang, H.-F. Song, M. Troyer, and A. A. Soluyanov, Comput. Phys. Commun. **224**, 405 (2018).

[62] U. Herath, P. Tavadze, X. He, E. Bousquet, S. Singh, F. Muoz, and A. H. Romero, Comput. Phys. Commun. **251**, 107080 (2019).

[63] The states near the Fermi energy (E_F) are mainly composed of Mo-4d and Te-5p orbitals. Due to the semicorrelated nature of Mo-4d orbitals, pure DFT fails to correctly describe the Angle-Resolved Photoemission Spectroscopy (ARPES) data and pressure dependence of quantum oscillation frequency measurements in $MoTe_2$ [43,44,64]. Adding an on-site Hubbard term (U_{eff}), the Hubbard term, on Mo-4d orbitals has been reported to solve this issue. Therefore, we consider $U_{\text{eff}} = 2.4$ eV as suggested by Xu *et al.* [43].

[64] S.-I. Kimura, Y. Nakajima, Z. Mita, R. Jha, R. Higashinaka, T. D. Matsuda, and Y. Aoki, Phys. Rev. B **99**, 195203 (2019).

[65] An animation showing the evolution of WPs as a function of $|\lambda/\lambda_0|$ is provided in the SM [50].

[66] I. Sodemann and L. Fu, Phys. Rev. Lett. **115**, 216806 (2015).

[67] Z. Z. Du, C. M. Wang, H.-Z. Lu, and X. C. Xie, Phys. Rev. Lett. **121**, 266601 (2018).

[68] Z. Z. Du, C. M. Wang, S. Li, H.-Z. Lu, and X. C. Xie, Nat. Commun. **10**, 3047 (2019).

[69] O. Matsyshyn and I. Sodemann, Phys. Rev. Lett. **123**, 246602 (2019).

[70] Due to the heavy computational cost of the Kubo formula and slow convergence of BCDM with respect to the k-mesh size, we first compute the Fermi surface by employing the tetrahedron method at a given k grid, and sample Berry curvature only at the reduced grid points near the Fermi surface. The convergence of BCDM was achieved at a k grid of size $278 \times 510 \times 130$ with Gaussian smearing, where the broadening width corresponds to ∼50 K.

[71] Q. Ma *et al.*, Nature (London) **565**, 337 (2019).

[72] In type-I Weyl semimetals, the major contribution to the BCDM comes from the WPs, whereas the rest of the Fermi surface makes a negligible contribution due to the isotropic group velocities near the WPs. Therefore, we notice a considerable change in the BCDM with respect to the chemical potential in T_d-$MoTe_2$ [41,73].

[73] J. I. Facio, D. Efremov, K. Koepernik, J.-S. You, I. Sodemann, and J. van den Brink, Phys. Rev. Lett. **121**, 246403 (2018).

[74] Note that the BCDM is a dimensionless quantity in three dimensions.

[75] Only four WPs are reported in Ref. [41] in contrast to the 12 (four W1 and eight W2) obtained in our case.

[76] We do not notice significant differences in the magnitudes of D_{ab} for the intermediate structures along the polarity reversal path, although new pairs of WPs get created/annihilated as a function of λ. This is due to the fact that most of the newly created WPs have relatively smaller tilt of Weyl cone compared to W1, thus yielding minimal changes to the overall BCDM.

[77] E. J. Sie *et al.*, Nature (London) **565**, 61 (2019).